Lab on a Chip

PAPER

View Article Online
View Journal | View Issue

Cite this: *Lab Chip*, 2025, **25**, 2390

Vascularized tumor-on-a-chip to investigate immunosuppression of CAR-T cells†

Rajul S. Bains, [a] Tara G. Raju,[a] Layla C. Semaan,[a] Anton Block,[a] Yukiko Yamaguchi,[cd] Saul J. Priceman,[cd] Steven C. George ‡*[ab] and Venktesh S. Shirure ‡*[a]

Chimeric antigen receptor (CAR)-T cell immunotherapy, effective in blood cancers, shows limited success in solid tumors, such as prostate, pancreatic, and brain cancers due, in part, to an immunosuppressive tumor microenvironment (TME). Immunosuppression affects various cell types, including tumor cells, macrophages, and endothelial cells. Conventional murine-based models offer limited concordance with human immunology and cancer biology. Therefore, we have developed a human "tumor-on-a-chip" (TOC) platform to model elements of immunosuppression at high spatiotemporal resolution. Our TOC features an endothelial cell-lined channel that mimics features of an *in vivo* capillary, such as cell attachment and extravasation across the endothelium and into the TME. Using 70 kDa dextran and fluorescence-recovery-after-photobleaching (FRAP), we confirmed physiologic interstitial flow velocities (0.1–1 μm s^{-1}). Our device demonstrates that tumor-derived factors can diffuse in the opposite direction of interstitial flow to reach the endothelium up to 200 μm away, and at concentrations as high as 20% of those at the tumor margin. M2-like immunosuppressive macrophages and endothelial cells affect prostate tumor cell growth, clustering, and migration. M2-like macrophages also induce PD-L1 and inhibit ICAM-1 gene expression on the adjacent endothelium in a pattern that limits CAR-T cell extravasation and effector function. This observation is abrogated in the presence of the anti-PD-L1 drug atezolizumab. These results provide mechanistic insight for *in vivo* observations showing limited CAR-T cell extravasation and effector function in solid tumors. Furthermore, they point to a specific role of M2 macrophages in driving CAR-T cell migration into and within the TME and could prove useful in the development of novel therapies to improve solid tumor CAR-T cell therapies.

Received 19th December 2024,
Accepted 16th April 2025

DOI: 10.1039/d4lc01089b

rsc.li/loc

Introduction

In chimeric antigen receptor (CAR)-T cell immunotherapy, T-cells from patients are isolated and genetically engineered to express tumor-specific CARs, expanded *ex vivo*, and reinfused into the patient to target antigen-expressing tumor cells.[1] This therapy has revolutionized the treatment of blood-based cancers; however, most patients with solid tumors (*e.g.*, prostate, pancreatic, and brain) respond poorly due to multiple factors. These include, but are not limited to: 1) a lack of tumor-specific antigen targets; 2) poor persistence following CAR-T cell infusion; and 3) decreased effector function of reinfused CAR-T cells within solid tumors.[2] A key feature that contributes to the latter is immunosuppression in the tumor microenvironment (TME).[3]

Immunosuppression can invoke an array of mechanisms and involves both cancer and non-cancer cell types (*e.g.*, tumor-associated macrophages, regulatory T cells, myeloid-derived suppressor cells, tumor-associated neutrophils, and stromal cells).[4] Among the cell types involved, M2 tumor-associated macrophages are most notable for their extensive TME infiltration and secretion of IL-10, TGF-β, and other factors that drive immunosuppression.[4] Immunosuppression results in impaired CAR-T cell attachment to the endothelium, extravasation across the endothelium, tumor infiltration, and effector function (*i.e.*, tumor cell killing). A more complete understanding of the underlying immunosuppressive mechanisms is necessary to develop

[a] *Department of Biomedical Engineering, University of California, Davis, Davis, CA, 95616, USA. E-mail: vsshirure@ucdavis.edu*
[b] *Department of Surgery, University of California, Davis,, Sacramento, CA, 95817, USA*
[c] *Department of Medicine, KSOM/NCCC Center for Cancer Cellular Immunotherapy Research, University of Southern California, Los Angeles, CA, 90098, USA*
[d] *Department of Hematology & Hematopoietic Cell Transplantation, City of Hope, Duarte, CA, 91010, USA*

† Electronic supplementary information (ESI) available. See DOI: https://doi.org/10.1039/d4lc01089b

‡ Authors contributed equally.

counterstrategies to enhance CAR-T cell persistence, tumor infiltration, and effector function in solid tumors.

The multi-step CAR-T cell homing and extravasation cascade is a sequence of events in which circulating CAR-T cells exit the vasculature and migrate into neighboring tissues. Essential biomolecules in this paradigm include intercellular adhesion molecule-1 (ICAM-1; CD54),[5] vascular cell adhesion molecule-1 (VCAM-1; CD106),[6] P-selectin (CD62P),[7] and E-selectin (CD62E).[7] These proteins are present on the vascular endothelium and facilitate the initial capture, rolling, adhesion, and extravasation of CAR-T cells from the vascular lumen to the adjacent interstitial space. Tumor-associated immunosuppression is linked with the downregulation of these proteins, but the precise mechanisms are unknown.[8,9]

Immune checkpoints (*e.g.*, PD-1, CTLA-4) are an additional family of proteins expressed on cytotoxic T cells involved in immune regulation.[10] When engaged with the respective cognate binding partner (*e.g.*, PD-L1 binds to PD-1), the effector function of the cytotoxic T cell is compromised. This regulatory mechanism, while normally serving to modulate immune responses, can be hijacked by solid tumors to evade immune surveillance and facilitate tumor growth and progression. Checkpoint inhibitors, such as atezolizumab (PD-L1 blocking antibody), have shown clinical efficacy in a small subset of patients with solid tumors.[11] PD-L1 can be expressed by numerous cells in the TME, including the endothelium; however, there is limited understanding of how PD-L1 expression on the tumor-adjacent vascular endothelium is impacted by the TME.

Mouse models of tumor biology have significantly advanced our understanding of immune processes; however, they exhibit limited concordance with the human immune response due to differences in cytokine signaling and adhesion molecule expression. For instance, inflammatory stimuli like tumor necrosis factor (TNF)-α increase P-selectin synthesis in mouse endothelial cells (ECs), whereas in human ECs, TNF-α primarily induces E-selectin expression,[12,13] highlighting key species-specific differences. Additionally, immunodeficient mouse models fail to capture the complexity of immune-tumor interactions and often overestimate therapeutic efficacy. While alternative 2D *in vitro* systems, such as parallel plate flow chambers or Boyden chambers, provide a human-relevant platform, they lack the 3D tissue architecture and dynamic flow conditions necessary to simulate all steps of immune cell extravasation. As CAR-T cell therapies continue to evolve, more physiologically relevant models are urgently needed to bridge the gap between preclinical testing and clinical translation.

Microfluidic-based organ-on-a-chip platforms that utilize human cells offer an *in vitro* alternative capable of replicating key features of the multicellular, complex 3D physiological architecture that more closely mimics *in vivo* human tissue and cancer.[14,15] These model systems utilize fine control of hydrostatic pressure to manipulate fluid flow through microchannels, thus creating highly customizable, complex, and reproducible 3D cellular microenvironments. Several microfluidic platforms, including those we previously developed, incorporate vascularized models of tissues such as tumors, bone marrow, and cardiac systems to study effects of drugs.[16–18] While organ-on-a-chip systems have demonstrated immune cell trafficking in response to exogenously added cytokines,[18,19] their ability to recapitulate trafficking dynamics shaped by the local immunosuppressive microenvironment remains poorly characterized. Immune cell trafficking is a central feature of the tumor microenvironment and involves a series of complex orchestrated events—a challenge that current platforms have yet to fully recapitulate.

In this study, we have created a "tumor-on-a-chip" (TOC) platform to specifically probe mechanisms associated with immunosuppression and the endothelium within the solid tumor TME. To accomplish this, our TOC includes a perfusable compartment lined by a confluent vascular endothelium adjacent to a tumor compartment that contains tumor cells and M2-like macrophages. This platform enables daily observation and tracking of growth of individual tumor cells. Our results demonstrate that M2-like macrophages affect tumor cell (prostate cancer cell line DU145) growth, limit CAR-T cell extravasation and effector function in solid tumors, and points to a specific role of M2-like macrophages in suppression of CAR-T cell therapy.

Experimental

Cell culture

The Human prostate cancer cell line DU145 (ATCC HTB-81) was cultured in RPMI-1640 (Thermo Fisher Scientific, Cat: 11875093) with 10% fetal bovine serum (FBS, Hyclone, SH30070.03). As previously described, wild type (WT) DU145 was lentivirally transduced to overexpress prostate stem cell antigen (PSCA+).[20]

As detailed in previous studies, endothelial colony-forming cell-derived (ECFC) endothelial cells (ECs) were extracted from umbilical cord blood.[17,21] ECs were fed endothelial growth medium (EGM-2; Lonza) and expanded to passage five before use. Some EC lines were lentivirally transduced to constitutively express green fluorescent protein (GFP).[17]

The CAR-T cells were derived following a protocol approved by the Institutional Review Board at City of Hope (Los Angeles, CA). The T cells were expanded and then lentivirally transduced with PSCA– or CD19-CAR as previously described[20] (Fig. S1†). The transduced cells were cryopreserved and shipped to UC Davis. A day prior to experimentation, CAR-T cells were cultured in X-VIVO-15 (Lonza) + 10% FBS (complete X-VIVO) supplemented with 78 IU mL^{-1} IL-2 (Biolegend, Cat: 501409) and 0.5 ng mL^{-1} IL-15 (Biolegend, Cat: 570302) to allow CAR-T cell activation.

Human CD14+ monocytes were isolated from the peripheral blood mononuclear cell (PBMC) fraction of peripheral blood using standard methods following a

protocol approved by the Institutional Review Board at City of Hope (Los Angeles, CA). The monocytes were cryopreserved in CryoStor CS5 (StemCell Technologies) and shipped to UC Davis. Monocytes were differentiated into M2-like macrophages using previously described methods.[22] In brief, monocytes were thawed and cultured for 4 days with RPMI-1640 + 10% FBS + M-CSF (BioLegend, Cat: 574802) at 20 ng mL^{-1}. Majority of the monocytes adhered to the bottom surface. Then, the media was replaced with fresh culture media supplemented with M-CSF, IL-4 (BioLegend, Cat: 574002), IL-6 (BioLegend, Cat: 570802), and IL-13 (BioLegend, Cat: 571102); all factors were at 20 ng mL^{-1} concentration. After 4–6 days, differentiated M2-like macrophages were lifted using DPBS (Gibco, Cat: 14190250) + 1 mM EDTA (ThermoFisher, Cat: J75793) and used in experimentation.

Fluorescence labelling of cells

CellTracker Orange CMRA dye (ThermoFisher, Cat: C34551) was used to label DU145 tumor cells, and CellTracker Green CMFDA dye (ThermoFisher, Cat: C7025) was used to label CAR-T cells. All labelling followed a standard workflow: cells were lifted, resuspended in DPBS (with ions) containing 3 μM of the fluorescent probe, incubated at 37 °C for 30 minutes, washed twice with DPBS (without ions), and prepared for loading.

Device design and experimental strategy

Our microfluidic TOC platform design features five parallel compartments (Fig. 1); a similar design was used in previous studies.[23,24] The parallel compartments communicate with each other through pore-like structures (30–50 microns in width), which are large enough to allow soluble mediators and cells to pass. For this study, the central chamber (ch1, Fig. 1B and C) is lined with a confluent layer of endothelial cells to mimic a capillary. Two reservoirs, made by cutting cryovials into cylinders and each capable of holding up to 1.5 mL of media, were attached to ch1 (Fig. 1A). The two adjacent interstitial chambers (ch2A,B, Fig. 1B and C) included the cancer cells and M2-like macrophages. Finally, the two outermost peripheral chambers (ch3A,B, Fig. 1B and C) serve as a lymphatic drainage or collection system. These chambers are connected to reservoirs made from 200 μL pipette tips (Fig. 1A). A hydrostatic pressure differential between chambers ch1 and ch3A,B drives interstitial fluid flow through ch2A,B into the lymphatic chambers (ch3A,B). This differential is regulated and maintained by adjusting the liquid height in the reservoirs connected to ch1 and ch3. The PDMS-based microfluidic device was fabricated using an SU-8 master mold created *via* softlithography, as previously described in detail.[21,25] After fabrication, cryovials were attached as reservoirs for ch1.

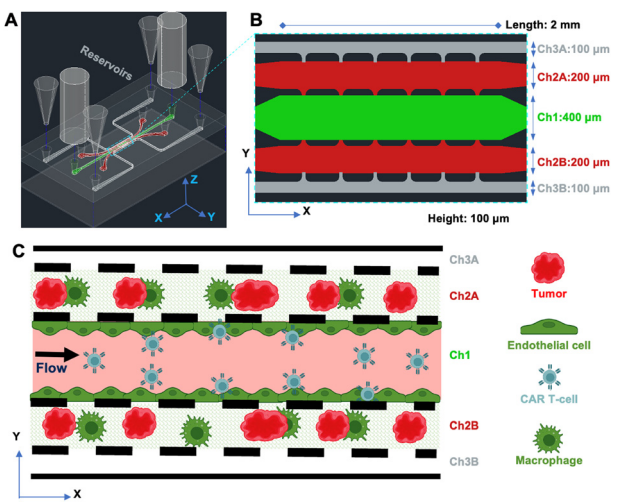

Fig. 1 Prostate tumor-on-a-chip (TOC) model. A) An isometric view of the TOC platform. Cylindrical cryovials were used as the reservoirs of ch1 (green), and micropipette tips were used as the reservoirs of ch3A, B (grey). B) A top-down schematic of our TOC platform featuring five parallel fluidic lines. C) A graphical representation of the device with its cellular components. ch1 is coated with endothelial cells to create a capillary; ch2A,B are loaded with tumor cells and macrophages in a fibrin extracellular matrix (ECM); ch.3A,B serve as the peripheral lymphatic chambers that collect interstitial fluid flow. CAR-T cells are perfused through ch1.

Device loading with cells

The fibrinogen solution was prepared by dissolving 10 mg mL^{-1} fibrinogen from bovine plasma (Sigma-Aldrich, Cat: F8630-10G) in DPBS (without ions) at 37 °C. DU145 prostate cancer cells (WT or PSCA+) at 3 million cells per mL were mixed with or without M2-like macrophages at the same concentration in fibrinogen. The fibrinogen-cell mixture was mixed with 0.9 μL bovine plasma thrombin (Sigma-Aldrich, Cat: T4648-1KU) at 50 U mL^{-1} and quickly loaded into ch2 of the device, typically within one minute. During this time frame, the fibrin mixture retains sufficient fluid-like properties, enabling low-pressure loading and uniform cell distribution, a method successfully used in our previous studies.[16–18,21,23] The devices were then incubated at 37 °C for 30–40 minutes to allow complete gel formation. Ch1 was then coated with gelatin (15 μL of 0.2% gelatin, Sigma-Aldrich, Cat: G1890-100G), which was subsequently replaced with ECs at 25 million cells per mL suspended in EGM-2.[18] ECs were allowed to attach to the device for 4–5 hours, and the unattached ECs were then washed. The device was fed with EGM-2 on day zero while EGM-2 without vascular endothelial growth factor (VEGF) and fibroblast growth factor (FGF) was used for rest of the experiment. Aprotinin (2 μg mL^{-1}), a broad plasmin inhibitor, was added to all reagents throughout experimentation to minimize fibrin degradation. For a specific experimental conditions, on day 1, the devices were pre-treated with 10 μg mL^{-1} atezolizumab (Tecentriq, Genentech), an anti-PD-L1 antibody, by perfusing it into the vascular central channel (ch1). On day 2, CAR-T cells were introduced into the vascular central channel (ch1) at 0.5 million per mL to model CAR-T extravasation and effector function.

Device staining with DAPI

For certain experiments, devices were fixed with formalin (Sigma-Aldrich, Cat: F5554-4L) by adding it to source reservoir of ch1 for 1 hour and then washing twice with DPBS (without ions). The devices were stained with 4′,6-diamidino-2-phenylindole (DAPI, ThermoFisher, Cat: D1306) at 2 μg mL^{-1} for 2 hours. The devices were washed with DPBS (without ions) to remove excess dye.

Acquisition and analysis of fluorescent images

We developed an image acquisition and analysis workflow to monitor the growth of individual tumors throughout the experiment. Devices were imaged daily using a confocal laser scanning microscope (FV1200 Fluoview, Olympus) connected to an image acquisition and analysis software (FV10-ASW, Olympus). Imaging was performed with a 10× objective, ensuring the same area remained in the field of view each day.

Fluorescent images were processed in ImageJ, where *z*-stacks were projected using maximum intensity algorithm. The images were then color-thresholded, and manual thresholding was performed when auto-thresholding was insufficient (*e.g.*, due to image artifacts). Thresholded images were analyzed using ImageJ's particle processing algorithm, which assigns a unique, sequential identity number to each tumor, determining their area and centroid coordinates (X, Y).

We developed a custom MATLAB script to facilitate tumor tracking. For each tumor identified on day 2 or in some cases day 0, the program calculated the Euclidean distance to every tumor in images from subsequent days (*e.g.* day 3–5). The identity numbers of tumors on day 3 and 5 were adjusted by assigning them to the closest tumor on day 2 or 0. This method ensured consistent tracking of each tumor (see ESI† methods and Fig. S3 for details). To calculate the rate of tumor growth, the normalized tumor areas for day 2, 3, and 5 (for CAR-T treated devices) or day 0–5 for other devices were fitted to a linear regression model. The slope of the fitted line was used to calculate the growth rate of each tumor.

Cell clustering and migratory calculations

Tumor cluster is defined as 3 or more cells in a circle of 10 μm radius. If the structure is large and continuous, it's counted as a single cluster. 'Migration' or inter-chamber movement of cells was defined as a ratio of cell-count in ch1 over the cell-count in ch2A and B. CellTracker Orange and nuclei-stained DAPI images were used for both calculations.

Endothelial cell gene expression

Endothelial cells in the device were washed with ion-free DPBS, and then removed by treating with accutase (ThermoFisher, Cat: A1110501) for 7–8 minutes at 37 °C; accutase was inactivated by adding EGM-2. Then, samples were resuspended in RNA Lysis Buffer + Triglycerides (TG) (StemCell Tech., Cat: 79040) for cell lysis or RNAlater (Invitrogen, Cat: 79040) following manufacturer's instructions for storage. Reverse transcription was performed using the High-Capacity cDNA Reverse Transcription Kit (Applied Biosystems, Cat: 4368814). qPCR was performed using the Fast SYBR Green Master Mix (Applied Biosystems, Cat: 4385612) with the respective human-specific primers for E-selectin (IDT, Hs.PT.58.20405152), ICAM (IDT, Hs.PT.58.4746364), VCAM (IDT, Hs.PT.58.20405152), and PD-L1 (IDT, Hs.PT.58.4665575). Beta-actin (IDT, Hs.PT.39a.22214847) was used as the house-keeping gene. qPCR was then performed on a QuantStudio 5 Real-Time PCR system (Applied Biosystems) using melt curve settings from the Fast SYBR Green protocol. Critical threshold values (Ct's) were quantified for each sample. ΔCt of a sample condition was found by subtracting the housekeeping gene Ct from gene-of-interest Ct. $\Delta\Delta C$ was then quantified by subtracting the average negative control ΔCt from the sample condition ΔCt. Gene-fold expression values are presented as $2^{-\Delta\Delta Ct}$.

Measurements of interstitial velocity and concentration profiles in the device

To characterize the flow and diffusion in the device, the device was loaded with fibrin as detailed above. The measurements of interstitial flow velocity were performed using fluorescence recovery after photobleaching (FRAP).[17,26] FITC-dextran (70 kDa, Sigma-Aldrich) was added to the central fluidic line (ch1) with a hydrostatic pressure gradient driving the dextran-fluid through tumor chambers (ch2A,B) into the lymphatic chambers (ch3A,B). Once the tumor chamber was filled with fluorescent dextran, a circular region of interest (ROI) of 10 μm diameter was bleached at predetermined locations in ch2A or 2B (Fig. 2A) with a short, strong laser (405 nm) pulse. Then, timelapse images were acquired at 4.76 frames per s for one minute. Using ImageJ, the displacement of centroid of the bleached region in each subsequent frame was measured, and the average of all displacements was used to calculate the interstitial velocity. To measure the hydraulic conductivity of fibrin gel in our platform, interstitial flow velocity was measured across ch2 at four different hydrostatic pressure gradients (0, 5, 10, and 20 mmH_2O) created by hydrostatic pressure differential in ch1 and ch3. Hydraulic conductivity (μm^2) was determined by a semi-empirical approach, in which the experimental velocities were matched in a computational (COMSOL) model[24] simulating pressure and fluid flow by varying the hydraulic conductivity and the best fit was chosen.

To evaluate concentration profiles of the tumor-secreted morphogens reaching the capillaries, the device was configured to establish interstitial fluid flow directed from the capillaries (ch1) toward lymphatic lines (ch3A,B), counter to the direction of diffusion of FITC-dextran. FITC-dextran was added to the lymphatic fluid lines (ch3A,B), while non-fluorescent media was added to ch1, generating a hydrostatic pressure gradient of 5 mmH_2O from ch1 to ch3A,B (Fig. 2G).

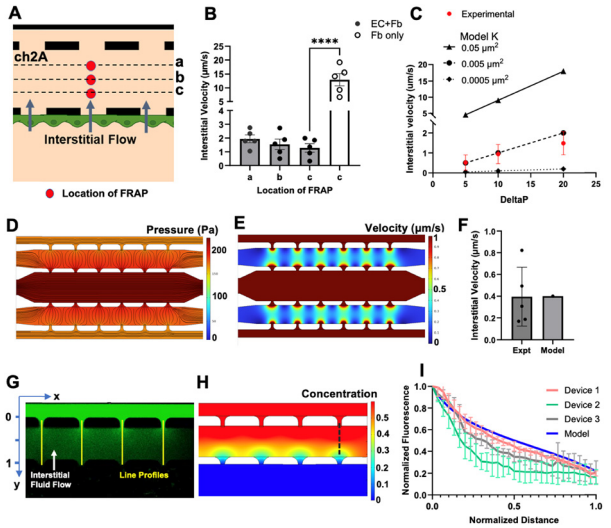

Fig. 2 TOC model recapitulates physiological interstitial flow and tumor morphogen gradients. A) Fluorescence-recovery-after-photobleaching (FRAP) was conducted in devices where fibrin was loaded into ch2A,B. FRAP locations along lines *c*, *b*, and *a* are respectively at 100, 140, and 180 μm from the endothelium. In devices without the endothelium, FRAP was conducted only at location *c*. B) The interstitial velocity was calculated at locations indicated in panel A at a pressure drop (ch1 to ch3A,B) of 20 mmH_2O. Data are from five replicates. C) Interstitial velocity at location c (panel A) was measured at various pressure drops. The hydraulic conductivity of EC-fibrin matrix in our device was determined using a computational model by varying the hydraulic conductivity to match experimentally measured interstitial velocities. D) Pressure, fluid streamlines, and E) velocity profiles were predicted for a pressure gradient of 5 mmH_2O by the computational model. F) The experimentally measured interstitial velocities under a 5 mmH_2O pressure gradient compared with those predicted by the computational model. Data are from five replicates. G) 70 kDa FITC-dextran was added to ch3A,B in devices loaded with ECs and fibrin. Interstitial flow (white arrow) against the direction of diffusion of FITC-dextran (green) was created under a pressure gradient of 5 mmH_2O. The fluorescent image was captured after 15 minutes and concentration line profiles (yellow lines) determined. H) Computational model simulations of dextran concentration (black dashed line is the location of concentration line profile. I) The experimentally measured concentration profiles (panel G) of three different devices were compared with that predicted by the computational model. The normalized distance values in the device are indicated in panel G. Each experimental curve is data from line plots at 4 pores of a device.

After 15 minutes, a steady-state fluorescent-dextran concentration profile was achieved, and fluorescence intensity as a function of position within ch2 was quantified using ImageJ (Fig. 2I).

Statistics

Statistical analysis and data fitting were performed using GraphPad Prism (10.3.0). Unless otherwise noted, data is presented as mean ± standard deviation (SD) with individual data points ($n \geq 3$). Statistical significance is indicated as follows: (*) $p < 0.05$, (**) $p < 0.01$, (***) $p < 0.001$, and (****) $p < 0.0001$. Ordinary one-way ANOVA with a Tukey's multiple comparison *post hoc* analysis or unpaired *t*-tests was used to analyze effects of a single factor. A mixed-effects model with Geisser–Greenhouse correction and Sidak's multiple comparisons test were used for comparing the fluorescent tumor areas over time.

Results

TOC characterization

We first characterized interstitial flow and the hydraulic conductivity in our TOC. The interstitial flow velocity in three positions (*a*, *b*, and *c*; Fig. 2A and B) for a pressure head of 20 mmH_2O were not statistically different (1.9 ± 0.5, 1.7 ± 0.6, and 1.3 ± 0.5 μm s^{-1}, respectively). In the absence of the endothelium (fibrin only), the interstitial flow increased by approximately one order of magnitude to 11 ± 3 μm s^{-1} (Fig. 2B).

To model velocity profiles through EC-fibrin gels, the hydraulic conductivity of the tissue was a required. Interstitial fluid velocities were measured under varying hydrostatic pressure gradients and compared with computational model predictions generated using different hydraulic conductivity values. The best-fitting value, 5×10^{-15} m^2, was selected (Fig. 2C). A 5 mmH_2O hydrostatic pressure drop (ch1 to ch3A,B) produced interstitial flow velocities of <1 μm s^{-1}, consistent with *in vivo* velocities in both normal and cancer tissue.[27,28] The experimentally measured velocities aligned closely with model predictions (Fig. 2F). The computational model also predicted pressure and velocity profiles within the device (Fig. 2D and E).

We next measured and simulated the concentration profile of 70 kDa dextran in the TOC under a pressure head of 5 mmH_2O (ch1 to ch3) and ch3 as the constant source of dextran. We measured the fluorescence intensity along a line from the edge of the lymphatic chamber (ch3) to the edge of the endothelium in four different locations. Dextran diffuses from ch3 (high concentration) to ch1 (low concentration) against the direction of interstitial to create a steady concentration profile in which the concentration of dextran at the endothelium is approximately 20% of the source. This experimental observation is confirmed by the computational model (Fig. 2G–I).

Tumor cell growth and migration

We next examined the growth and migration of tumor cells in the presence of the endothelium and M2-like macrophages. For this study, we used the DU145 prostate tumor cell line, transduced with lentivirus to stably express prostate stem cell antigen (PSCA), which was confirmed by flow cytometry (Fig. S1A†). Both DU145-wildtype (WT) and DU145-PSCA exhibited the same proliferation, migration, and cluster formation at baseline (Fig. 3A–C). Next, we tested the TOC, which incorporated endothelial cells in ch1 or M2-like macrophages (Fig. S1B and C†) in ch2A,B, along with the tumor cells. The endothelium coated in ch1 remains confluent for up to five days (Fig. S2†). The presence of M2-

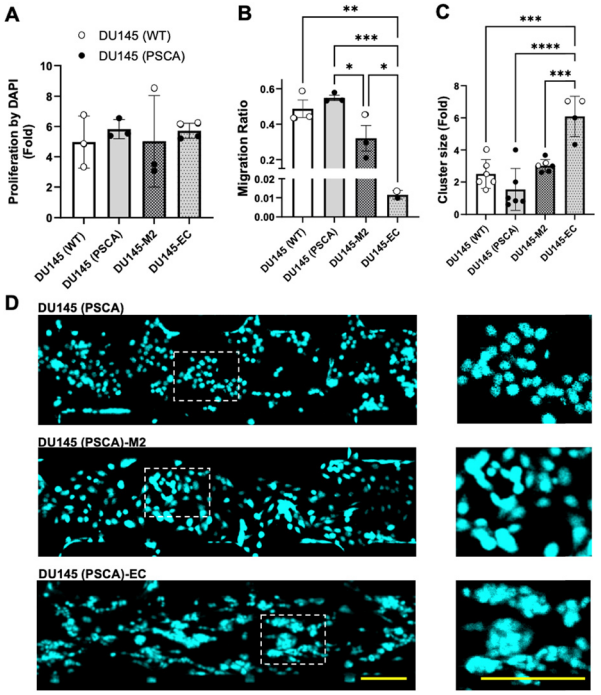

Fig. 3 Endothelial cells and M2 macrophages modulate DU145 prostate cancer cell behavior and growth. DU145 prostate cancer cells were cultured in the TOC for 6 days under three conditions: alone, with macrophages, or with ECs. The devices were then stained with DAPI to visualize their nuclei. A) The ratio of cell nuclei on day 6 (DAPI-stained) and on day 0 (brightfield imaging) was calculated to assess proliferation. B) The ratio of number of cells in ch1 to ch2 on day 6 was used to assess migration. C) The average number of DAPI-stained nuclei per cluster. A–C) The data are from at least three replicates, except for the DU-145-EC conditions, where the data are from two replicates. D) Representative images of ch2A visualized through DAPI staining reveal differences in spatial organization and clustering under different co-culture conditions. Insets highlight regions of interest showing cluster morphology. The scale bar is 100 μm.

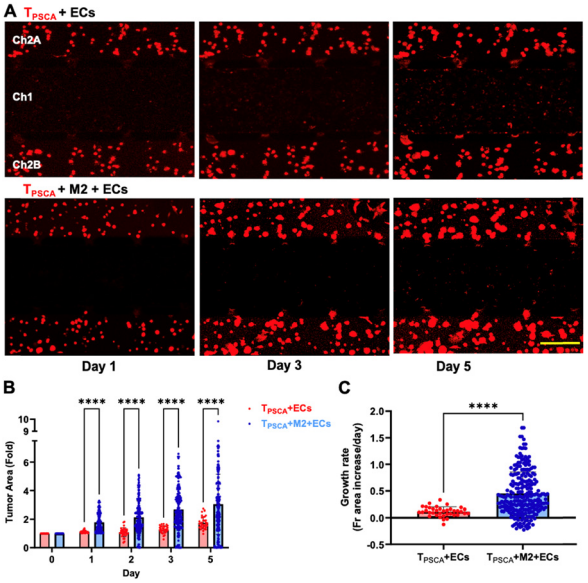

Fig. 4 M2-like macrophage in a tri-culture with DU145 and ECs enhance tumor growth. The proliferation of PSCA transduced DU145 prostate tumor cells (T_{PSCA}) were evaluated in co-culture with ECs and in tri-culture with M2-like macrophages and ECs. A) Representative fluorescent images depict tumor area (red fluorescence) under different co-culture conditions. The first row shows growth in co-culture with endothelial cells (ECs) alone, while the second row depicts growth in tri-culture with both ECs and M2-like macrophages. The scale bar 200 μm. B) Tumor area of individual tumors in the TOC was determined using a tumor-tracking algorithm. C) Tumor growth rates of individual tumors were calculated by regression analysis of tumor area. B and C) Data from at least three replicates.

like macrophages or endothelial cells alone did not impact proliferation of tumor cells (Fig. 3A) as assessed by total cell number (DAPI staining), but the presence of endothelial cells significantly reduced migration (Fig. 3B) and increased clustering (Fig. 3C and D).

DAPI staining does not permit live tracking and often inaccurately counts closely clustered tumors, such as observed in the presence of endothelial cells (Fig. 3D). To address these limitations, we employed fluorescent tracking to measure the fluorescent area of tumors. We observed a significant increase in total fluorescence, consistent with increased tumor growth (Fig. 4A), in the presence of both endothelial cells and M2-like macrophages. To examine this phenomenon in greater detail, we tracked the growth of all individual tumor cells from Day 0 in the presence of endothelial cells alone or endothelial cells and M2-like macrophages (ESI† methods and Fig. S3). This analysis shows a wide distribution of growth depending on the tumor cell, particularly in the presence of endothelial cells and M2-like macrophages (*i.e.*, not all tumor cells proliferate, while others proliferate at a high rate) (Fig. 4B). The growth rate of each tumor cell varies widely, but the presence of the M2-like macrophage clearly stimulates overall growth of the tumor (Fig. 4C).

These data show that tumor growth in the vascularized TOC is largely confined to the tumor chamber and trackable with fluorescent readouts, thus enabling subsequent studies with daily tracking and precise assessment of treatment effects at the single-tumor level.

CAR T cell trafficking and effector function

We next tested the ability of CAR-T cells to traffic from the vascular compartment, into the tumor chamber, and limit tumor growth. DU145-PSCA tumor growth is negative in the presence of PSCA-CAR T cells, consistent with tumor cell killing (Fig. 5). In contrast, tumor growth was maintained in the presence of non-targeted CAR-T cells. We next tested the hypothesis that the M2-like macrophage could limit CAR-T cell trafficking and effector function. The presence of M2-like macrophages significantly augments tumor growth (Fig. 6A–C), and limits CAR-T cell number in the tumor chamber (Fig. 6D). We next hypothesized that the effect of the M2-like macrophage may be due to enhanced PD-L1 expression in the TME, based on our own studies as well as in the field.[29,30] The presence of the PD-L1 blocking antibody,

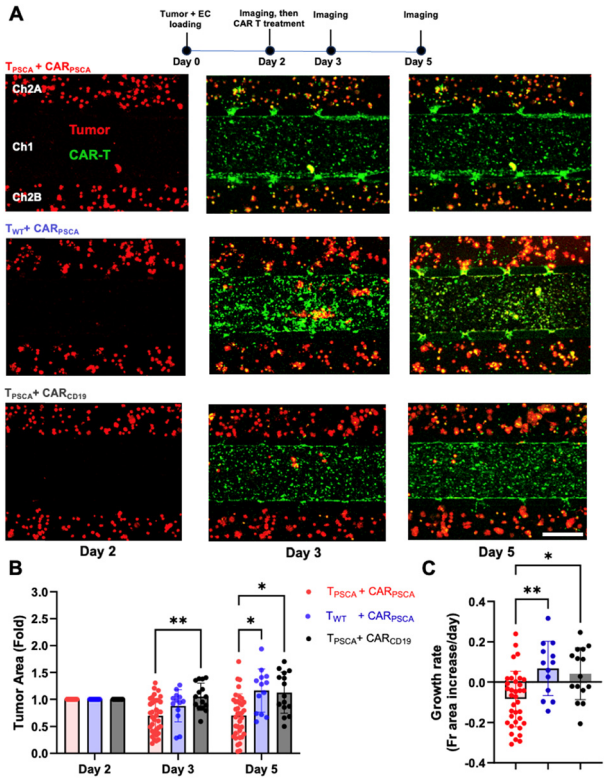

Fig. 5 PSCA-targeting CAR-T cells selectively target PSCA-expressing DU145 tumor cells. Interactions between PSCA-targeting CAR-T (CAR_{PSCA}) or CD19-targetting CAR-T cells (CAR_{CD19}) and PSCA transduced DU145 prostate cancer cells (T_{PSCA}) or wild type DU145 cells (T_{WT}) was evaluated in devices loaded with ECs. A) Timeline of imaging and CAR-T cell treatment with representative fluorescent images of tumor cells (red) treated with CAR-T cells (green). Scale bar 200 μm. B) Tumor area of individual tumors in ch2A and 2B of the TOC was found using our *tumor-tracking algorithm*. C) Tumor growth rates of each individual tumors were calculated by regression analysis of tumor areas. B and C) Data from at least three replicates.

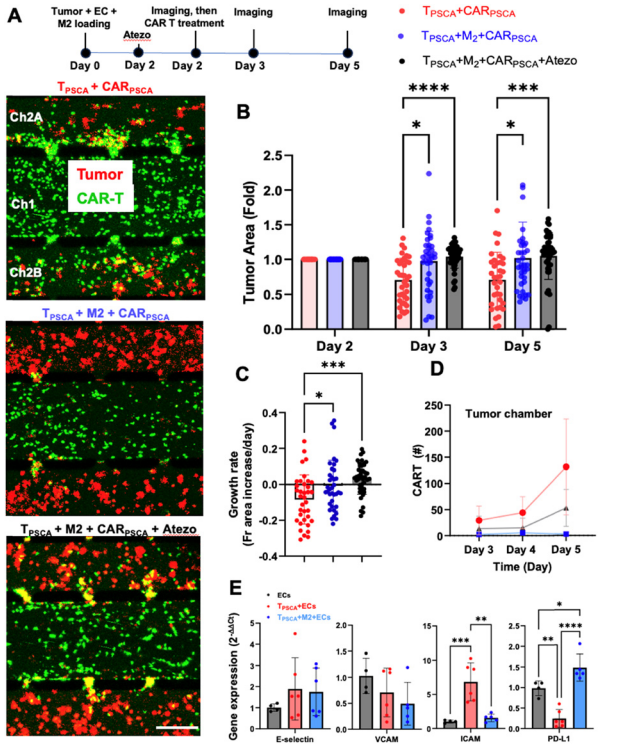

Fig. 6 The impact of M2-like macrophages and atezolizumab (anti-PD-L1) pre-treatment on CAR-T cells function in the TOC. PSCA transduced DU145 prostate tumor cells (T_{PSCA}) were cultured with ECs and optionally with M2-like macrophages. These devices were treated on day 2 with PSCA-targeting CAR-T cells (CAR_{PSCA}; green fluorescence) alone or CAR_{PSCA} and atezolizumab (an anti-PDL-1 mAb). A) Representative fluorescent images of PSCA-targeting CAR-T cells (green fluorescence) and PSCA-expressing DU145 tumor cells (red fluorescence) acquired on day 5. The scale bar is 200 μm. B) Tumor area of individual tumors in ch2A and 2B of the TOC was found using our *tumor-tracking algorithm*. C) Tumor growth rates of each individual tumors were calculated by regression analysis of tumor areas. D) Number of CAR-T cells infiltrating the tumor chamber (ch2A, B) quantified over time. B–D) Data from at least 3 replicates. E) The ECs from the ch1 of the device were extracted for gene expression analysis. The expression of endothelial adhesion and extravasation markers (E-selectin, VCAM-1, and ICAM-1) and immune checkpoint ligand PD-L1 were quantified. Data is from at least four replicates.

atezolizumab, does not impact the enhanced tumor growth in the presence of M2-like macrophages (Fig. 6A–C), but augmented the number of the CAR-T cells in the tumor chamber, particularly on Day 4 (Fig. 6D).

Based on our observation that large biomolecules can diffuse against physiologic interstitial flow and the crosstalk between tumor cells and endothelial cells (Fig. 2), we hypothesized that DU145 tumor cells could potentially impact gene expression in endothelial cells. In the presence of tumor cells, gene expression of ICAM-1 and PD-L1 in the endothelium was significantly increased and decreased, respectively; this trend was completely reversed in the presence of M2-like macrophages (Fig. 6E) and is consistent with the pattern of CAR-T cell trafficking and tumor growth.

Discussion

Our study presents a 3D *in vitro* microfluidic-based model of the TME that includes an endothelialized vascular channel and specifically mimics elements of immunosuppression by incorporating M2-like macrophages into the tumor compartment. Given these features, we used the model to probe mechanisms of immunosuppression that impact CAR-T cell trafficking and effector function. Using the prostate cancer cell line DU145 (WT and overexpressing PSCA) and CAR-T cells specific for the PSCA antigen, our model made the following observations: 1) tumor cells and/or macrophages can signal the adjacent endothelium against interstitial flow to influence phenotype; 2) similarly, the endothelium can signal to the tumor cell impacting cell migration and organization patterns; 3) CAR-T trafficking, including endothelial cell attachment, extravasation, and tumor cell killing can be readily observed and quantified in the model system; and 4) M2-like macrophages can stimulate tumor growth and suppress CAR-T endothelial attachment

and effector function, partly through increased expression of ICAM-1 and PD-L1 by the endothelial cell. Together, our results present a scalable 3D *in vitro* model of the immunosuppressive TME. The model can be used to observe cellular trafficking between the vasculature and tumor and demonstrates that M2-like macrophages contribute to reduced CAR-T cell effector function by altering the expression of ICAM-1 and PD-L1 in the endothelium.

Endothelial cell attachment and extravasation

Leukocyte adhesion (capture and rolling) to and extravasation through the vascular endothelium is a hallmark feature of inflammation, and the proteins involved are well-described. The selectins (P- and E-) play key roles in the initial capture and rolling, while adhesion molecules such as ICAM-1 and VCAM-1 play important roles in the firm adhesion.[31] Less well-understood is the role of PD-L1 expression on the endothelial cell during inflammation. PD-L1 is the ligand for the PD-1 receptor which is expressed on a host of leukocytes including endogenous and CAR-T cells. PD-1 activation induces a host of responses in the cytotoxic T cell, including inhibiting proliferation, reducing pro-inflammatory cytokine (TNFα, IL-2, IFNγ) production, suppressing glycolysis, and broadly inducing exhaustion.[32]

PD-L1 expression by the endothelium has been reported and associated with suppressed CD8+ T cell cytotoxicity; but, these studies did not investigate the contribution of the TME.[33,34] A particularly important exception is the recent study by Chi and colleagues[35] who presented a TOC with an endothelial barrier and demonstrated strong endothelial expression of PD-L1 adjacent to a TME that included tumor cells and fibroblasts. Our study demonstrates that the DU145 prostate cancer cell line alone can impact both CAR-T attachment and activation by simultaneously increasing ICAM-1 expression and decreasing PD-L1 expression. This initial response may contribute to an early and robust immune response to identify and eliminate cancer cells. However, in the presence of M2-like macrophages, this trend in ICAM-1 and PD-L1 expression is flipped (Fig. 6E) such that CAR-T cell trafficking into tumors simultaneously decreased (Fig. 6D), thus facilitating tumor growth (Fig. 6A–C). We observed that atezolizumab augments the number of CAR-T cells in the tumor chamber, suggesting that PD-L1 expression on the endothelium is a key mechanism by which M2-like macrophages contributes to immunosuppression. However, the observation that atezolizumab does not restore tumor growth inhibition in the presence of CAR-T cells suggests that CAR-T cells that do reach the tumor chamber encounter a refractive immunosuppressive environment created by M2-like macrophages that likely involve mechanisms beyond PD-L1 expression, at least in our system. It is noteworthy that our prior studies using 2D co-cultures indicate that atezolizumab did blunt function of PD-L1 by M2-like macrophages and restored CAR-T cell killing of tumor cells,[29] but this effect of atezolizumab was limited in an *in vivo* syngeneic mouse model (unpublished data), further supporting the need for more elaborate 3D culture systems like our TOC platform to more comprehensively reflect the TME. Nonetheless, this result suggests that both macrophages and endothelial cells may be targeted in the TME to limit tumor progression.

Immunosuppression in the TME

To model elements of immunosuppression in the TME, we chose M2-like macrophages, as they are notable for their extensive TME infiltration, and secretion of IL-10, arginase, TGFβ and other chemokines (*e.g.*, CCL1) that drive immunosuppression.[36,37] Our results demonstrate that the presence of M2-like macrophages can impact the expression of ICAM-1 and PD-L1 in the endothelial cell. This observation is consistent with decreased CAR-T cell attachment, extravasation, and tumor cell killing observed in the TOC. However, it remains unclear whether this effect is driven by soluble mediator(s) secreted from macrophages, such as TGFβ,[38] directly impacting endothelial cells and/or indirectly through altered mediator production by tumor cells. Further investigation is warranted to clarify these mechanisms.

Additionally, other cells can contribute to immunosuppression in the TME including stromal cells,[39,40] regulatory T cells,[41] myeloid derived suppressor cells,[42] and tumor associated neutrophils.[43] These cell types could be incorporated into alternate models of the TOC alone or in combination to explore the full spectrum of immunosuppression. There have been several previous reports to model features of immunosuppression in a complex 3D *in vitro* environment,[35,44–48] and has been recently reviewed.[49] Each of these models demonstrates specific features of the complex immunosuppressive TME. The simplest models include tumor cells within a hydrogel adjacent to a compartment that allows immune cells to migrate into the TME.[46,47] More advanced models such as the model presented in the current study or by Wang and colleagues[45] introduce CAR-T cells matched with tumor specific antigens. Several of the models have also included an endothelial barrier,[35,44] similar that shown by our current model. The unique features of our model are the incorporation of M2-like macrophages, and the inclusion of controlled and physiological levels of interstitial flow.

Transport of soluble mediators in the TME

Fluid filtration from the capillary into adjacent tissue occurs preferentially at the start of a capillary where the combination of hydrostatic and osmotic pressures are favorable. At the end of a capillary in normal tissue, hydrostatic pressure decreases enough to reverse this flow, and small amounts of fluid are reabsorbed. This physiological environment is maintained in smaller tumors, but elevated interstitial pressure in larger tumors effectively eliminates convection in the interstitial space except at the tumor margins.[50] As such, our TOC model simulates fluid

filtration in the first portion of the capillary in small tumors. Under these conditions, we demonstrate experimentally that under physiological interstitial flow, tumor-derived mediators can be transported by diffusion towards the endothelium at concentrations that are ~20% of a tumor cell as far as 200 μm away. This phenomenon was confirmed by altered gene expression of ICAM-1 and PD-L1 (Fig. 6F). The observation that most cells are <100 μm from the nearest capillary[51] suggests that tumor-derived soluble mediators can impact leukocyte (including T cell) attachment and activation/inactivation to the endothelium over the entire length of the capillary, even the earliest portion where filtration of fluid and absorption into the lymphatics would favor the transport of tumor-derived mediators away from the endothelium.

Tumor-derived morphogens are typically 5–50 kDa in size (*e.g.*, VEGF – 45 kDa, bFGF – 17 kDa, SDF-1 – 8 kDa, IFG – 7.6 kDa, EGF – 6 kDa, Wnt – 39–46 kDa, and TGF-β – 25 kDa). We utilized 70 kDa dextran as a proxy for possible morphogens secreted by the TME (Fig. 2G). Since the molecular diffusion coefficient is inversely related to the molecular weight, we reasoned that if 70 kDa dextran could diffuse against interstitial flow and reach the endothelium, smaller proteins would be able to as well.

Finally, although the fluorescence measurements exhibit some variability (Fig. 2I), this is likely due to the sensitivity of fluorescence method to factors such as slight positional shifts of the stage within an individual device, and small variations in the interstitial fluid flow between devices. Nonetheless, the data consistently demonstrate that a significant portion of tumor-secreted morphogens successfully reach the endothelial cells against the direction of interstitial flow.

Tumor cell migration and organization

We observed an increase in tumor cell clustering and reduced migration in the presence of the endothelium. This observation is consistent with the long-standing association between tumor growth and vascularization.[52] Interestingly, M2-like macrophages had limited effect on tumor cell migration and clustering, but when added to tumor cells and the endothelium were able to stimulate tumor cell growth. This observation, consistent with the anti-inflammatory, pro-growth phenotype associated with M2-like macrophages,[53] and in addition to CAR-T cell trafficking and tumor cell killing, highlights additional features of the TME that can be observed using our TOC platform.

Limitations and opportunities of the TOC platform

While our TOC platform provides a robust approach for studying CAR-T cell therapies, it currently lacks the additional cell types discussed above. The tumor tracking algorithm developed for the TOC performs well under low cell density conditions, where tumor cells occupy less than 1% of the device volume, thus minimizing mergers of nearby cells. At higher cell densities, however, frequent mergers and larger clusters can pose challenges, as centroid-based tracking becomes less reliable due to significant shifts in centroid positions. As such we recommend using the algorithm at low to moderate cell densities, with manual validation for specific experimental conditions prior to broader implementation.

Despite these limitations, the platform's ability to track individual tumor responses and its customizability for integrating additional cell types make it an ideal tool for investigating immunosuppression. It can be used to explore combination therapies aimed at reducing immunosuppression, such as STAT3 inhibition[54] (targeting macrophages) and PD-L1 inhibition[55,56] to enhance CAR T-cell therapy. Additionally, it is well-suited for testing the efficacy of engineered TCR T-cell treatments, tumor-infiltrating lymphocyte (TIL) therapy, and mechanisms of drug resistance.

Conclusion

Our study presents a TOC model that mimics specific features of the TME, including a confluent vascular endothelium, physiological interstitial flow, prostate cancer cells, and immune suppression *via* the incorporation of M2-like macrophages. The model can be used to observe cell trafficking and growth in the TME at high spatiotemporal resolution. Specifically, we used the TOC to investigate the role of the M2-like macrophage to limit CAR-T trafficking and effector function, enhancing tumor cell growth. Consistent with *in vivo* observations, our initial results suggest that M2-like macrophages can significantly augment tumor growth at baseline and inhibit CAR-T-induced tumor cell killing. This observation is due, in part, to a reversal in the expression pattern of ICAM-1 and PD-L1 on the endothelium to limit CAR-T attachment and migration into the TME. Our results demonstrate that our TOC can simulate key features of immunosuppression in the TME, suggesting that both the macrophage and the endothelium could be targeted to enhance CAR-T cell trafficking and effector function in solid tumors.

Data availability

The algorithm used to determine the growth rates of individual tumors and/or tumor cells as shown in Fig. 4–6 is described in detail in the ESI† document.

Conflicts of interest

There are no conflicts to declare.

Acknowledgements

The authors would like to thank Dr. Bhupinder Shergill, Dr. Pete Sariano, Dr. Matthew B. Curtis, and Evan Cirves for technical assistance. We would also like to thank the UC Davis Centre for Nano and Micro Manufacturing (CNM2),

where a part of the microfabrication was performed. This work was supported by a UC Davis Academic Federation Innovative Developmental Award (VSS), a PCF Tactical Award (SJP), and a DOD Idea Development and Expansion Award (SJP, W81XWH-21-1-0354, PC200485).

References

1 S. Feins, W. Kong, E. F. Williams, M. C. Milone and J. A. Fraietta, *Am. J. Hematol.*, 2019, **94**, S3–S9.
2 S. M. Albelda, *Nat. Rev. Clin. Oncol.*, 2024, **21**, 47–66.
3 A. Johnson, M. Townsend and K. O'Neill, *Cell*, 2022, **11**, 3626.
4 Y. Tie, F. Tang, Y.-Q. Wei and X.-W. Wei, *J. Hematol. Oncol.*, 2022, **15**, 61.
5 C. Lawson and S. Wolf, *Pharmacol. Rep.*, 2009, **61**, 22–32.
6 J. M. Cook-Mills, *Mol. Immunol.*, 2002, **39**, 499.
7 R. P. McEver, *Cardiovasc. Res.*, 2015, **107**, 331–339.
8 P. Leone, E. Malerba, N. Susca, E. Favoino, F. Perosa, G. Brunori, M. Prete and V. Racanelli, *Front. Immunol.*, 2024, **15**, 1367875.
9 J. Fang, Y. Lu, J. Zheng, X. Jiang, H. Shen, X. Shang, Y. Lu and P. Fu, *Cell Death Dis.*, 2023, **14**, 586.
10 M. C. Brunner-Weinzierl and C. E. Rudd, *Front. Immunol.*, 2018, **9**, DOI: **10.3389/fimmu.2018.02737**.
11 J. Tabernero, F. Andre, J.-Y. Blay, A. Bustillos, S. Fear, S. Ganta, D. Jaeger, M. Maio, L. Mileshkin and I. Melero, *ESMO Open*, 2022, **7**, 100419.
12 Z. Liu, J. J. Miner, T. Yago, L. Yao, F. Lupu, L. Xia and R. P. McEver, *J. Exp. Med.*, 2010, **207**, 2975–2987.
13 L. Yao, H. Setiadi, L. Xia, Z. Laszik, F. B. Taylor and R. P. McEver, *Blood*, 1999, **94**, 3820–3828.
14 N. Del Piccolo, V. S. Shirure, Y. Bi, S. P. Goedegebuure, S. Gholami, C. C. Hughes, R. C. Fields and S. C. George, *Adv. Drug Delivery Rev.*, 2021, **175**, 113798.
15 V. S. Shirure, C. C. W. Hughes and S. C. George, *Annu. Rev. Biomed. Eng.*, 2021, **23**, 141–167.
16 D. E. Glaser, M. B. Curtis, P. A. Sariano, Z. A. Rollins, B. S. Shergill, A. Anand, A. M. Deely, V. S. Shirure, L. Anderson, J. M. Lowen, N. R. Ng, K. Weilbaecher, D. C. Link and S. C. George, *Biomaterials*, 2022, **280**, 121245.
17 V. S. Shirure, A. Lezia, A. Tao, L. F. Alonzo and S. C. George, *Angiogenesis*, 2017, **20**, 493–504.
18 V. S. Shirure, S. Yechikov, B. S. Shergill, T. Dehghani, A. V. Block, H. Sodhi, A. Panitch and S. C. George, *Lab Chip*, 2023, **23**(13), 3050–3061.
19 J. I. Kennedy, S. P. Davies, P. W. Hewett, A. L. Wilkinson, Y. H. Oo, W.-Y. Lu, A. J. El Haj and S. Shetty, *Front. Cell Dev. Biol.*, 2024, **12**, 1359451.
20 S. J. Priceman, E. A. Gerdts, D. Tilakawardane, K. T. Kennewick, J. P. Murad, A. K. Park, B. Jeang, Y. Yamaguchi, X. Yang, R. Urak, L. Weng, W.-C. Chang, S. Wright, S. Pal, R. E. Reiter, A. M. Wu, C. E. Brown and S. J. Forman, *Onco Targets Ther*, 2018, **7**, e1380764.
21 M. L. Moya, Y. H. Hsu, A. P. Lee, C. C. Hughes and S. C. George, *Tissue Eng., Part C*, 2013, **19**, 730–737.
22 J. C. Zarif, J. R. Hernandez, J. E. Verdone, S. P. Campbell, C. G. Drake and K. J. Pienta, *Biotechniques*, 2016, **61**(1), 33–41.
23 V. S. Shirure, B. Ye, M. B. Curtis, A. Lezia, M. M. Goedegebuure, P. Goedegebuure, R. Aft, R. C. Fields and S. C. George, *Lab Chip*, 2018, **18**, 3687–3702.
24 K.-C. Weng, Y. K. Kurokawa, B. S. Hajek, J. A. Paladin, V. S. Shirure and S. C. George, *Tissue Eng., Part C*, 2020, **26**, 44–55.
25 Y. H. Hsu, M. L. Moya, P. Abiri, C. C. Hughes, S. C. George and A. P. Lee, *Lab Chip*, 2013, **13**, 81–89.
26 R. K. Jain, R. J. Stock, S. R. Chary and M. Rueter, *Microvasc. Res.*, 1990, **39**, 77–93.
27 J. M. Rutkowski and M. A. Swartz, *Trends Cell Biol.*, 2007, **17**, 44–50.
28 H. Dafni, T. Israely, Z. Bhujwalla, L. Benjamin and M. Neeman, *Cancer Res.*, 2002, **62**, 6731–6739.
29 Y. Yamaguchi, J. Gibson, K. Ou, L. S. Lopez, R. H. Ng, N. Leggett, V. D. Jonsson, J. C. Zarif, P. P. Lee, X. Wang, C. Martinez, T. B. Dorff, S. J. Forman and S. J. Priceman, *J. ImmunoTher. Cancer*, 2022, **10**, e004400.
30 F. Guo, W. Kong, D. Li, G. Zhao, M. Anwar, F. Xia, Y. Zhang, C. Ma and X. Ma, *Eur. J. Med. Res.*, 2024, **29**, 357.
31 D. N. Granger and E. Senchenkova, in *Inflammation and the Microcirculation*, Morgan & Claypool Life Sciences, 2010.
32 M. J. Kim and S.-J. Ha, *Front. Cell Dev. Biol.*, 2021, **9**, 767466.
33 W.-J. Chen, X.-F. Hu, M. Yan, W.-Y. Zhang, X.-B. Mao and Y.-W. Shu, *Atherosclerosis*, 2016, **244**, 108–112.
34 M. M. Mazanet and C. C. W. Hughes, *J. Immunol.*, 2002, **169**, 3581–3588.
35 C.-W. Chi, Y.-H. Lao, A. H. Rezwanuddin Ahmed, S. He, T. Merghoub, K. W. Leong and S. Wang, *Lab Chip*, 2024, **24**, 396–407.
36 L. Cassetta and J. W. Pollard, *Nat. Rev. Drug Discovery*, 2018, **17**, 887–904.
37 E. Peranzoni, J. Lemoine, L. Vimeux, V. Feuillet, S. Barrin, C. Kantari-Mimoun, N. Bercovici, M. Guérin, J. Biton and H. Ouakrim, *Proc. Natl. Acad. Sci. U. S. A.*, 2018, **115**, E4041–E4050.
38 F. Du, X. Qi, A. Zhang, F. Sui, X. Wang, C. G. Proud, C. Lin, X. Fan and J. Li, *Exp. Mol. Med.*, 2021, **53**, 1366–1378.
39 E. Sahai, I. Astsaturov, E. Cukierman, D. G. DeNardo, M. Egeblad, R. M. Evans, D. Fearon, F. R. Greten, S. R. Hingorani and T. Hunter, *Nat. Rev. Cancer*, 2020, **20**, 174–186.
40 M. A. Lakins, E. Ghorani, H. Munir, C. P. Martins and J. D. Shields, *Nat. Commun.*, 2018, **9**, 1–9.
41 A. Schmidt, N. Oberle and P. H. Krammer, *Front. Immunol.*, 2012, **3**, DOI: **10.3389/fimmu.2012.00051**.
42 V. Kumar, S. Patel, E. Tcyganov and D. I. Gabrilovich, *Trends Immunol.*, 2016, **37**, 208–220.
43 H. Luo, N. Ikenaga, K. Nakata, N. Higashijima, P. Zhong, A. Kubo, C. Wu, C. Tsutsumi, Y. Shimada, M. Hayashi, K. Oyama, S. Date, T. Abe, N. Ideno, C. Iwamoto, K. Shindo, K. Ohuchida, Y. Oda and M. Nakamura, *J. Exp. Clin. Cancer Res.*, 2024, **43**, 258.
44 J. Lee, S.-E. Kim, D. Moon and J. Doh, *Lab Chip*, 2021, **21**, 2142–2152.

45 X. Wang, I. Scarfò, A. Schmidts, M. Toner, M. V. Maus and D. Irimia, *Adv. Sci.*, 2019, **6**, 1901829.
46 Y. Ando, E. L. Siegler, H. P. Ta, G. E. Cinay, H. Zhou, K. A. Gorrell, H. Au, B. M. Jarvis, P. Wang and K. Shen, *Adv. Healthcare Mater.*, 2019, **8**, 1900001.
47 K. Paterson, S. Paterson, T. Mulholland, S. B. Coffelt and M. Zagnoni, *IEEE Open J. Eng. Med. Biol.*, 2022, **3**, 86–95.
48 H.-Y. Mu, C.-M. Lin, L.-A. Chu, Y.-H. Lin, J. Li, C.-Y. Liu, H.-C. Huang, S.-L. Cheng, T.-Y. Lee, H. M. Lee, H.-M. Chen, Y.-J. Tsai, Y. Chen and J.-H. Huang, *Adv. Healthcare Mater.*, 2024, **13**, 2302268.
49 Y. Lee, J. Min, S. Kim, W. Park, J. Ko and N. L. Jeon, *Adv. Healthcare Mater.*, 2025, **14**(1), e2401927.
50 R. K. Jain and L. T. Baxter, *Cancer Res.*, 1988, **48**, 7022–7032.
51 G. Helmlinger, F. Yuan, M. Dellian and R. K. Jain, *Nat. Med.*, 1997, **3**, 177–182.
52 D. Hanahan and R. A. Weinberg, *Cell*, 2011, **144**, 646–674.
53 N. Wang, H. Liang and K. Zen, *Front. Immunol.*, 2014, **5**, 614.
54 M. Kortylewski and D. Moreira, *Cancer Immunol., Immunother.*, 2017, **66**, 979–988.
55 T. Gargett, W. Yu, G. Dotti, E. S. Yvon, S. N. Christo, J. D. Hayball, I. D. Lewis, M. K. Brenner and M. P. Brown, *Mol. Ther.*, 2016, **24**, 1135–1149.
56 L. B. John, C. Devaud, C. P. Duong, C. S. Yong, P. A. Beavis, N. M. Haynes, M. T. Chow, M. J. Smyth, M. H. Kershaw and P. K. Darcy, *Clin. Cancer Res.*, 2013, **19**, 5636–5646.